



Article

Additive Manufacturing of a 316L Steel Matrix Composite Reinforced with CeO₂ Particles: Process Optimization by Adjusting the Laser Scanning Speed

Omar O. Salman ^{1,*}, Alexander Funk ¹, Anja Waske ¹ , Jürgen Eckert ^{2,3} and Sergio Scudino ¹

¹ Institute for Complex Materials, IFW Dresden, Helmholtzstraße 20, D-01069 Dresden, Germany; a.funk@ifw-dresden.de (A.F.); a.waske@ifw-dresden.de (A.W.); s.scudino@ifw-dresden.de (S.S.)

² Erich Schmid Institute of Materials Science, Austrian Academy of Sciences, Jahnstraße 12, A-8700 Leoben, Austria; juergen.eckert@unileoben.ac.at

³ Department Materials Physics, Montanuniversität Leoben, Jahnstraße 12, A-8700 Leoben, Austria

* Correspondence: o.o.salman@ifw-dresden.de; Tel.: +49-351-46591807

Received: 28 December 2017; Accepted: 13 February 2018; Published: 15 February 2018

Abstract: The synthesis of novel materials by additive manufacturing requires the optimization of the processing parameters in order to obtain fully-dense defect-free specimens. This step is particularly important for processing of composite materials, where the addition of a second phase may significantly alter the melting and solidification steps. In this work, a composite consisting of a 316L steel matrix and 5 vol.% CeO₂ particles was fabricated by selective laser melting (SLM). The SLM parameters leading to a defect-free 316L matrix are not suitable for the production of 316L/CeO₂ composite specimens. However, highly-dense composite samples can be synthesized by carefully adjusting the laser scanning speed, while keeping the other parameters constant. The addition of the CeO₂ reinforcement does not alter phase formation, but it affects the microstructure of the composite, which is significantly refined compared with the unreinforced 316L material.

Keywords: additive manufacturing; selective laser melting; processing parameters; stainless steel

1. Introduction

Material synthesis by additive manufacturing (AM) has recently emerged as a flexible processing tool for the fabrication of components with intricate geometries and superior properties [1]. Among the different AM technologies, selective laser melting (SLM) represents an optimal choice for the production of highly-dense metallic parts because of the use of high-energy laser beams capable to fuse/weld metallic particles layer by layer [2,3]. Additionally, SLM processing leads to remarkable differences in terms of microstructures and properties compared with conventional manufacturing processes, like casting [4–6]. High temperature gradients, fast moving of the laser beam, and rapid solidification are characteristic features of SLM, which can crucially affect microstructures and properties of the SLM parts [2,7].

A wide variety of materials, including Al-based alloys, steels, and metallic glasses [5,7,8], has been fabricated by SLM. In particular, 316L steel synthesized by SLM has been extensively investigated because of its excellent corrosion and oxidation resistance under severe environments [9–11]. Recent efforts have been focused on the fabrication of stainless steel matrix composites [12,13]. For example, AlMangour et al. [14,15] studied the effect of powder preparation as well as of size and volume fraction of TiC reinforcements on the microstructure and mechanical properties of 316L, while Hao et al. [16] and Wei et al. [17] optimized the SLM processing parameters to fabricate a hydroxyapatite/316L composite. The addition of reinforcing particles—such as SiC, TiC, TiB₂, and Al₂O₃—to stainless steel

can further enhance mechanical and wear properties at moderate and high temperatures, and expand the range of potential applications of these composites to aerospace and biomedical industries [18,19].

Two main features play a decisive role for determining the final microstructure and the mechanical properties of composites synthesized by SLM: the first is related to the processing parameters, such as laser power, laser scan speed, hatch distance, hatch layer thickness, and laser spot size [20] and the second is associated with the characteristics of the reinforcing particles, including particle size and morphology, and their dispersion within the matrix [21]. A uniform distribution of the reinforcing particles in a matrix-reinforcement powder mixture is a prerequisite for its homogeneous distribution in the final bulk composite. Ball milling can be successfully used for the preparation of homogeneous particle mixtures. The uniform distribution of the reinforcement achieved by ball milling, however, it is usually accompanied by a change of the powder morphology resulting from the high energy impacts between particles and milling media [22,23], which in turn may influence the solidification characteristics and the properties of the composite material after SLM [23].

Due to the addition of the second phase and the change of the powder morphology, the SLM processing parameters leading to defect-free specimens of the unreinforced matrix might not be suitable for the synthesis of fully-dense composites and the optimization of the parameters might be necessary [24–26]. Accordingly, the objective of this work is the optimization of the SLM processing parameters to produce defect-free 316L matrix composites reinforced with 5 vol.% CeO₂ particles. To achieve this aim, different scanning speeds have been employed and the resulting phases, microstructures and densification of the SLM parts have been investigated. The present steel-matrix composite belongs to the family of oxide dispersion strengthened (ODS) alloys, where oxide particles, such as Y₂O₃, CeO₂, Al₂O₃, and TiO₂ [27], are dispersed into a metallic matrix in order to achieve elevated temperature strength, creep, and resistance against radiation [28,29].

2. Materials and Methods

Gas-atomized 316L stainless steel powder (Realizer GmbH) with spherical morphology and average particle size of 36 µm (Figure 1a,b) and CeO₂ powder (chemPUR) with size in the range of 0.5–1 µm were used for the present experiments. Composite powder mixtures consisting of the 316L matrix and 5 vol.% CeO₂ were prepared by ball milling in order to ensure the homogeneous distribution of the reinforcing phase. Ball milling was carried out for 2 h using a Retsch PM 400 (Retsch, Haan, Germany) planetary ball mill with hardened steel vials and balls at a ball-to-powder weight ratio of 6:1 and a milling velocity of 100 rpm. To avoid an excessive temperature rise inside the vial during milling, the rotation was paused for 15 min after every 15 min milling. SLM processing was performed using an SLM 250 HL device (SLM Solutions, Lübeck, Germany) equipped with a Yb-YAG laser. Cylindrical samples with 3.5 mm diameter and 7 mm length were built on a 316L substrate plate using the following parameters: laser power 175 W, layer thickness 30 µm, hatch spacing 120 µm, and hatch style rotation 79°. The scanning speed was varied in the range of 250–688 mm/s (688 mm/s being the optimized speed for the single-phase 316L). In order to minimize oxygen contamination, SLM processing was carried out under high purity argon atmosphere. Phase analysis was performed by X-ray diffraction (XRD) using a D3290 PANalytical X' PRO diffractometer with Co-K α radiation ($\lambda = 0.17889$ nm). The density of the samples was measured by the Archimedes principle and by X-ray computed tomography (XCT). XCT scans with voxel size of 5 µm were carried out using a General Electric Phoenix Nanotom m device (General Electric, New York, NY, USA). The microstructure of the samples was investigated by scanning electron microscopy (SEM; Leo Gemini 1530, Carl Zeiss, Jena, Germany). Samples for SEM investigations were mechanically polished and chemically etched at room temperature for 7 min using an acidic water solution containing 2% HF and 8% HNO₃. The size distributions of the particles and cells were evaluated from the SEM micrographs by using the image analysis software ImageJ 1.X. Crystallographic orientation and grain size of the SLM samples were studied by EBSD (Brooker esprit, detector e flash-HR) using the ESPRIT.2.1 CrystAlign software [30]. The step size of the EBSD measurement was 1 µm. For EBSD mapping, the unreinforced 316L matrix

and composite samples were sectioned along the Y-Z plane (with X building direction). Room temperature quasistatic compression tests (strain rate = $8 \times 10^{-5} \text{ s}^{-1}$) were performed on cylindrical samples (7 mm length and 3.5 mm diameter) of the unreinforced 316L and 316L/CeO₂ composites using an Instron 5869 testing facility. The strain was measured directly on the samples using a Fiedler laser-extensometer. The compression tests for all specimens were intentionally stopped at 15% strain. A total of 10 specimens for unreinforced matrix and composite were tested in order to ensure the reproducibility of the results.

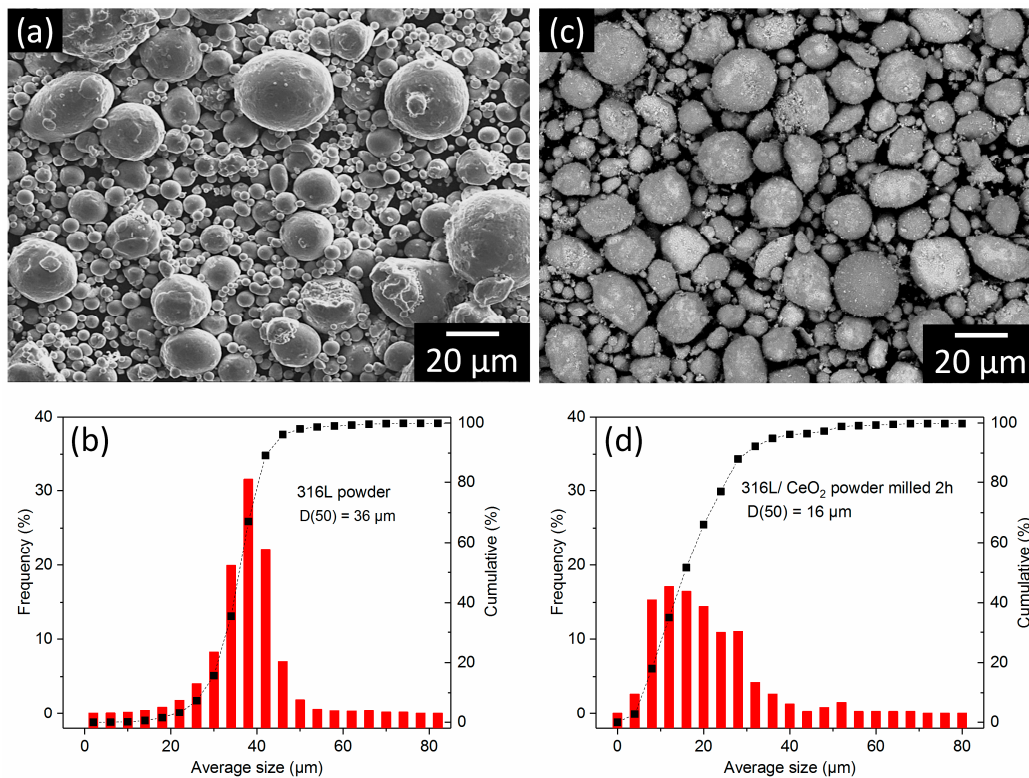


Figure 1. Powder morphology and particle size distribution for: (a,b) as-atomized pure 316L powder and (c,d) 316L/CeO₂ powder mixture ball milled for 2 h.

3. Results and Discussion

The optimized SLM parameters for the unreinforced 316L matrix (scanning speed 688 mm/s, laser power 175 W, layer thickness 30 µm, hatch spacing 120 µm, and hatch style rotation 79°) provide highly-dense specimens with a relative density of 99.9%, as demonstrated by the corresponding results in Figures 2a and 3a. On the other hand, the same parameters are not suitable for SLM processing of the 316L/CeO₂ powder mixture: the composite material is highly porous (relative density ~94%) with the CeO₂ phase (bright contrast in Figure 3b) mostly located at the interface between matrix and pores. Two main differences, which can explain this behavior, exist in the processing of the unreinforced matrix and 316L/CeO₂ powders: (i) the milling step used for the preparation of the homogeneous 316L/CeO₂ powder mixture and (ii) the presence of the CeO₂ second phase.

Milling can induce a significant change in the size and morphology of the powder, which in turn may influence the melting and solidification steps. Indeed, milling for 2 h drastically increases the size of the unreinforced 316L powder so that defect-free specimens can no longer be synthesized using the optimized parameters (not shown here). On the other hand, milling the 316L/CeO₂ powder mixture only slightly reduces the particle size compared to the as-atomized powder (Figure 1c,d). The effect of milling can, therefore, be neglected.

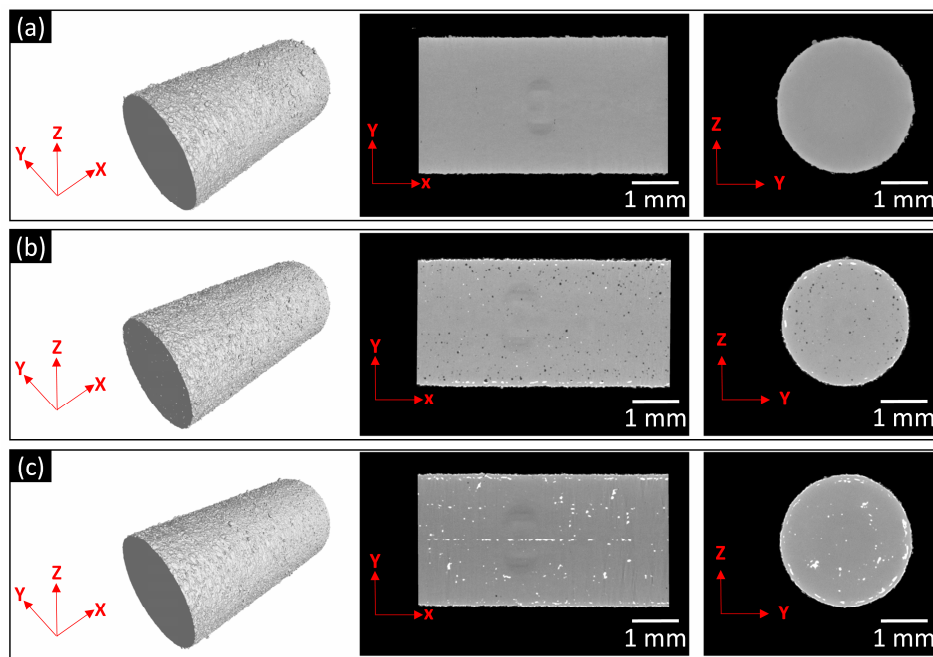


Figure 2. XCT images for: (a) an unreinforced 316L specimen synthesized by SLM with a scanning speed of 688 mm/s, (b) a 316L/CeO₂ composite synthesized at 350 mm/s, and (c) a 316L/CeO₂ composite synthesized at 488 mm/s. Note that the other processing parameters have been kept constant. The small bright particles in (b) and (c) are CeO₂ and the black dots in (b) are porosity.

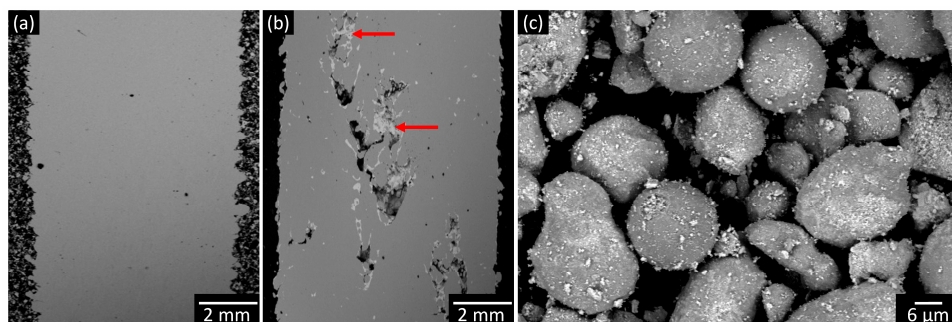


Figure 3. SEM micrographs for: (a) an unreinforced 316L specimen synthesized by SLM at 688 mm/s; (b) a 316L/CeO₂ composite synthesized at 688 mm/s; and (c) 316L/CeO₂ powder mixture ball milled for 2 h. The bright contrast indicated by red arrows in (b) and the small bright particles adhering to the large 316L particles in (c) are the CeO₂ phase.

The addition to the CeO₂ second phase most likely has the strongest impact for affecting powder melting and the subsequent solidification process. The presence of the CeO₂ particles on the surface of the 316L particles (Figure 3c) may absorb some of the laser energy input, making the energy insufficient to entirely melt the 316L particles. This behavior may preferentially raise the temperature on the particles surface, leading to surface melting, while the particle cores are still solid. Through this mechanism, necks are formed between the particles; however, due to the fast movement of the laser beam, the particles are only partially joined together and pores between solidified metallic agglomerates are left behind [31].

The use of a low laser power or a fast laser scanning speed usually leads to higher porosity during laser processing of 316L stainless steel [31]. Under these conditions, the energy input is decreased and the volume of the melt pool becomes smaller, leading to a discontinuous scan track smaller than the laser spot and to the occurrence of the balling phenomenon [32–35], where the laser penetration depth

is not deep enough to weld the neighboring layers [36]. To overcome this problem, the decrease of the laser scanning speed is recommended to achieve higher densification levels in SLM parts [37]. Lower scanning speeds, and thus the increase of the laser energy input, create a large melt pool and more powder particles are melted [38].

The scanning speed should be selected carefully in order to provide sufficient energy input capable to create a continuous track of molten liquid and a fully dense surface after solidification. The density of CeO_2 (7.65 g/m^3) is slightly lower than that of 316L (8 g/m^3) [39] and, consequently, the scanning speed should be fast enough to shorten the solidification time without giving the reinforcement particles time for floating on the top of the melt pool [17]. Decreasing the scanning speed to 350 mm/s, while keeping the other parameters constant, increases the relative density to 98% (Figure 2b); unfortunately, the CeO_2 particles are not homogeneously distributed and are mainly located at the edges of the sample. At such a low scanning speed, a large temperature gradient may exist between the center and the edge of the melt pool [40]. This may lead to a higher surface tension at the cooler edge, which may then be accompanied by the outward flow of the CeO_2 particles from the hot liquid to the edge of the pool, explaining the behavior observed in Figure 2b. This adverse effect can be mitigated by increasing the scanning speed to 488 mm/s (Figure 2c). SLM processing using this speed corresponds to sufficient energy density to fully melt the powder particles, avoiding the preferential location of the reinforcement particles along the sample edges. No crack or balling phenomena occur at this optimized speed and the 316L/ CeO_2 composite sample shows a very high relative density of 99.9% with rather well-distributed reinforcing particles.

Both the unreinforced 316L matrix and 316L/ CeO_2 composite consist of a single-phase austenite structure (Figure 4). The CeO_2 phase cannot be detected in all XRD patterns. This can be due to the melting and dissolution of the CeO_2 phase during SLM or because the small amount of reinforcement is below the detection limit of the instrument. The latter possibility is corroborated by the fact that no diffraction peaks of the CeO_2 phase are detected in the 316L/ CeO_2 milled powder. In addition, the CeO_2 particles are visible in the XCT image in Figure 2c, further supporting that the CeO_2 phase is not melted during the process. Because XCT analysis was carried out using a voxel size of $5 \mu\text{m}$, which sets the lowest limit for the detection of the second phase, it is surprising to observe the CeO_2 particles considering their small starting size ($0.5\text{--}1 \mu\text{m}$). The CeO_2 particles must, therefore, have been clustered during SLM processing to a size suitable for XCT analysis. This hypothesis is corroborated by the SEM micrographs shown in Figure 5: CeO_2 particles with size in the range of $30\text{--}200 \mu\text{m}$ are indeed formed in the 316L/ CeO_2 composite.

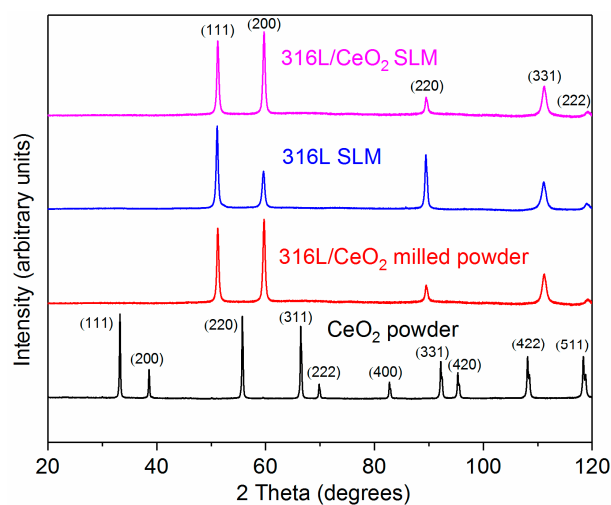


Figure 4. XRD patterns ($\lambda = 0.17889 \text{ nm}$) for pure CeO_2 powder, 316L/ CeO_2 powder mixture ball milled for 2 h, an unreinforced 316L specimen processed at 688 mm/s, and a 316L/ CeO_2 composite sample synthesized at 488 mm/s.

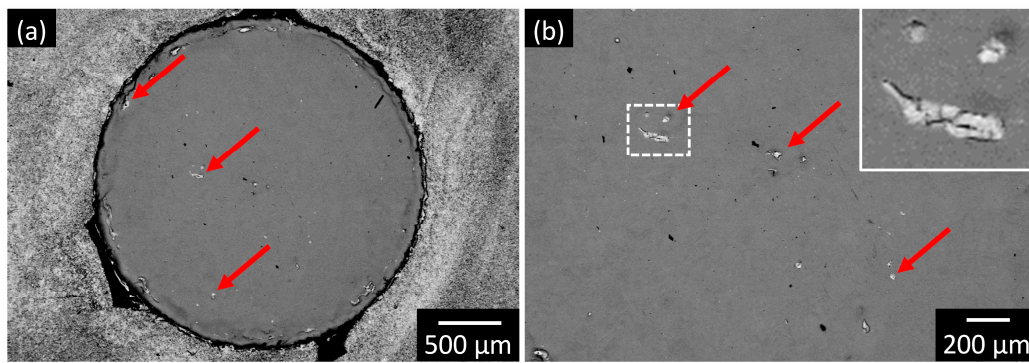


Figure 5. SEM micrographs for the 316L/CeO₂ composite synthesized by SLM at 488 mm/s: (a) overview showing the distribution of the CeO₂ particles; (b) view at higher magnification revealing that clustering of the CeO₂ particles occurs during SLM (see also the inset corresponding to the dashed box in (b)). The red arrows indicate the position of the CeO₂ particles.

Due to the high cooling rate characterizing materials processing by SLM (10^3 – 10^6 K/s), metastable phases and microstructures can be formed [6,8,41]. The present unreinforced 316L specimen displays a fine cellular microstructure (Figure 6a,b), in agreement with previous reports on 316L fabricated by SLM [42–44]. The addition of the CeO₂ reinforcement does not affect the formation of the cellular microstructure (Figure 6c–e); however, the CeO₂ phase induces significant microstructural refinement and decreases the cell size in the composite material with respect to the unreinforced matrix, as demonstrated by the cell size distributions shown in Figure 6f.

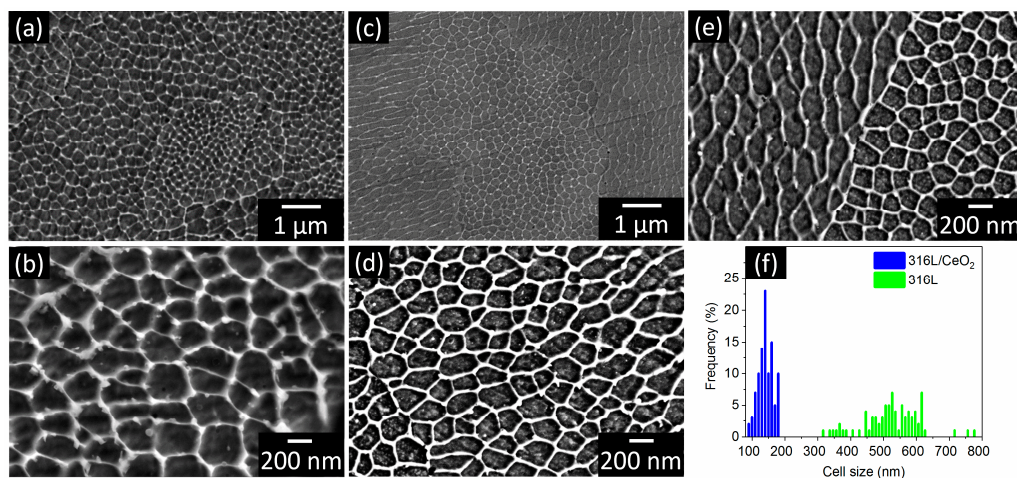


Figure 6. SEM images showing the cellular microstructure formed in (a,b) an unreinforced 316L specimen synthesized by SLM at 688 mm/s and (c–e) a 316L/CeO₂ composite synthesized at 488 mm/s; (f) Distribution of the cell size in the unreinforced 316L and 316L/CeO₂ composite.

Grain refinement occurs at a larger length scale as well. EBSD analysis reveals that the average grain size (calculated over more than 2300 grains) of the unreinforced 316L (45 ± 3 μm) is reduced in the 316L/CeO₂ composite to about 25 ± 2 μm (Figure 7). The CeO₂ particles are thus effective grain refiners, acting as heterogeneous nucleation sites and hindering the growth of both cells and grains [45]. The reduced grain size cannot be attributed to the reduced scanning speed used in the 316L/CeO₂ composite with respect to the unreinforced 316L. Slower scanning speed would increase the depth and volume of the molten pool, consequently raising the temperature and increasing the time needed for solidification. This, in turn, would give the grains more time to grow, leading to microstructural coarsening rather than refining, in agreement with the work of Dutta Majumdar et al. [46], who observed

the decrease of the grain size with increasing scanning speed in 316L steel processed by laser assisted rapid fabrication. The addition of the CeO₂ reinforcement has a significant influence on the yield strength (0.2% offset), which increases from 412 ± 7 MPa for the unreinforced 316L to 485 ± 4 MPa for the 316L/CeO₂ composite while retaining appreciable plastic deformation (Figure 8). The observed increase of strength can be ascribed to the load bearing capacity of the CeO₂ reinforcement [47] along with the Hall–Petch strengthening contribution resulting from structural refinement [48].

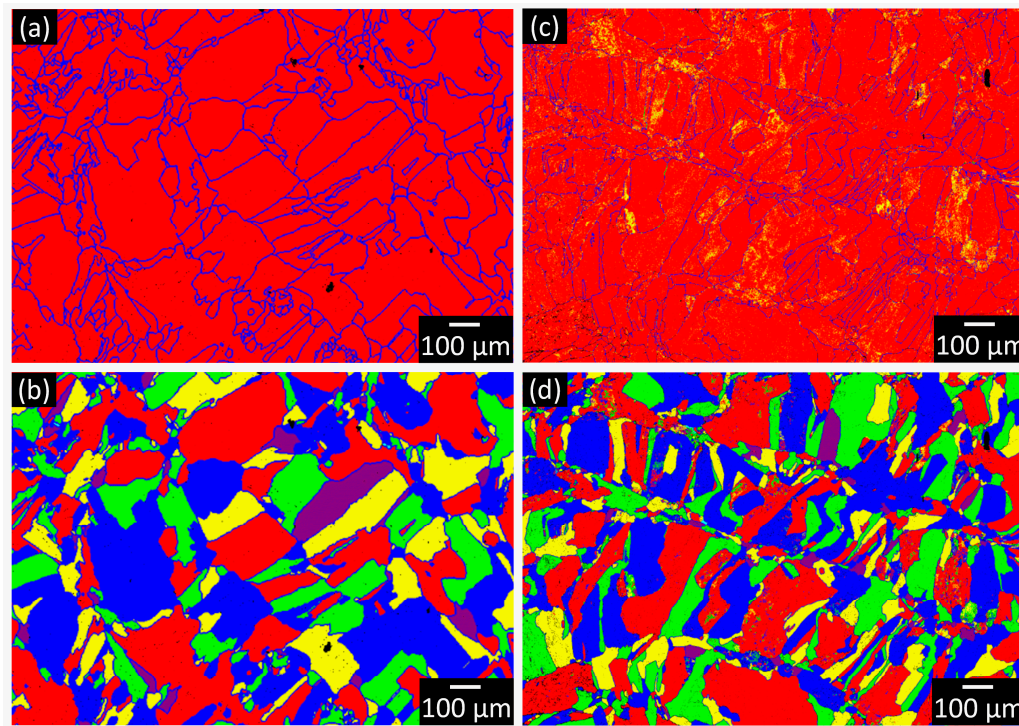


Figure 7. EBSD analysis for: (a,b) an unreinforced SLM 316L specimen synthesized at 688 mm/s and (c,d) a SLM 316L/CeO₂ composite processed at 488 mm/s. The small yellow particles in (c) are CeO₂.

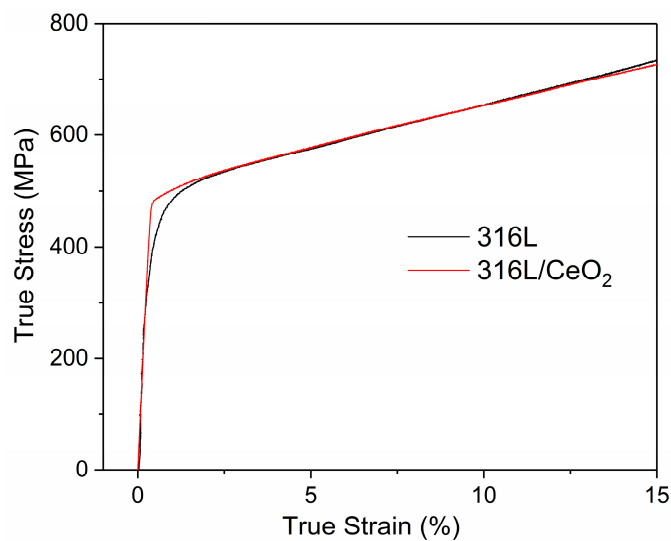


Figure 8. Room-temperature compressive stress–strain curves for the unreinforced SLM 316L specimen synthesized at 688 mm/s and SLM 316L/CeO₂ composite processed at 488 mm/s.

4. Conclusions

In summary, we have optimized the SLM processing of 316L/CeO₂ composites in order to achieve highly-dense defect-free specimens. This aim can be achieved without the need to explore the effect of the entire set of experimental parameters. Excellent specimens can be synthesized by carefully adjusting the laser scanning speed, while keeping the other parameters constant. The addition of the CeO₂ phase does not change the phase formation during solidification but it affects the microstructure of the composite, which is considerably refined compared with the unreinforced 316L material. The refined microstructure induces significant strengthening in the composite without deteriorating the plastic deformation. These preliminary results not only indicate that highly-dense 316L/CeO₂ composites with enhanced room-temperature strength can be synthesized by SLM, but also they open the possibility to extend the analysis of their properties to high temperatures, enlarging the possible applications of this type of composites.

Acknowledgments: The authors thank K.G. Prashanth and T. Gustmann for stimulating discussions. O.O.S. gratefully acknowledges the financial support from the Ministry of Higher Education & Scientific Research (MoHESR), Iraq. Additional support through the ERC Advanced Grant INTELHYB (grant ERC-2013-ADG-340025) is gratefully acknowledged.

Author Contributions: O.O.S. and S.S. conceived and designed the experiments; O.O.S. performed the experiments; O.O.S. and S.S. analyzed the data and wrote the paper; A.F., A.W., and J.E. contributed to the discussion of the results and to the writing of the paper.

Conflicts of Interest: The authors declare no conflict of interest.

References

1. Berman, B. 3-D printing the new industrial revolution. *Bus. Horiz.* **2012**, *55*, 155–162. [[CrossRef](#)]
2. Shifeng, W.; Shuai, L.; Qingsong, W.; Yan, C.; Sheng, Z.; Yusheng, S. Effect of molten pool boundaries on the mechanical properties of selective laser melting parts. *J. Mater. Process. Technol.* **2014**, *214*, 2660–2667. [[CrossRef](#)]
3. Santos, E.C.; Shiomi, M.; Osakada, K.; Laoui, T. Rapid manufacturing of metal components by laser forming. *Int. J. Mach. Tools Manuf.* **2006**, *46*, 1459–1468. [[CrossRef](#)]
4. Song, B.; Zhao, X.; Li, S.; Han, C.; Wei, Q.; Wen, S.; Liu, J.; Shi, Y. Differences in microstructure and properties between selective laser melting and traditional manufacturing for fabrication of metal parts: A review. *Front. Mech. Eng.* **2015**, *10*, 111–125. [[CrossRef](#)]
5. Prashanth, K.G.; Scudino, S.; Klauss, H.; Surreddi, K.B.; Löber, L.; Wang, Z.; Chaubey, A.K.; Kühn, U.; Eckert, J. Microstructure and mechanical properties of Al-12Si produced by selective laser melting: Effect of heat treatment. *Mater. Sci. Eng. A* **2014**, *590*, 153–160. [[CrossRef](#)]
6. Scudino, S.; Unterdörfer, C.; Prashanth, K.G.; Attar, H.; Ellendt, N.; Uhlenwinkel, V.; Eckert, J. Additive manufacturing of Cu-10Sn bronze. *Mater. Lett.* **2015**, *156*, 202–204. [[CrossRef](#)]
7. Taha, M.A.; Yousef, A.F.; Gany, K.A.; Sabour, H.A. On selective laser melting of ultra high carbon steel: Effect of scan speed and post heat treatment. *Materialwiss. Werkst.* **2012**, *43*, 913–923. [[CrossRef](#)]
8. Pauly, S.; Löber, L.; Petters, R.; Stoica, M.; Scudino, S.; Kühn, U.; Eckert, J. Processing of metallic glasses by selective laser melting. *Mater. Today* **2013**, *16*, 37–41. [[CrossRef](#)]
9. Kocabekir, B.; Kaçar, R.; Gündüz, S.; Hayat, F. An effect of heat input, weld atmosphere and weld cooling conditions on the resistance spot weldability of 316L austenitic stainless steel. *J. Mater. Process. Technol.* **2008**, *195*, 327–335. [[CrossRef](#)]
10. Sumita, M.; Hanawa, T.; Teoh, S.H. Development of nitrogen-containing nickel-free austenitic stainless steels for metallic biomaterials—Review. *Mater. Sci. Eng. C* **2004**, *24*, 753–760. [[CrossRef](#)]
11. Imbaby, M.; Jiang, K.; Chang, I. Net shape fabrication of stainless-steel micro machine components from metallic powder. *J. Micromech. Microeng.* **2008**, *18*, 115018. [[CrossRef](#)]
12. Das, K.; Bandyopadhyay, T.K.; Das, S. A review on the various synthesis routes of TiC reinforced ferrous based composites. *J. Mater. Sci.* **2002**, *37*, 3881–3892. [[CrossRef](#)]
13. Pagounis, E.; Lindroos, V. Processing and properties of particulate reinforced steel matrix composites. *Mater. Sci. Eng. A* **1998**, *246*, 221–234. [[CrossRef](#)]

14. AlMangour, B.; Grzesiak, D.; Yang, J.-M. Selective laser melting of TiB₂/316L stainless steel composites: The roles of powder preparation and hot isostatic pressing post-treatment. *Powder Technol.* **2017**, *309*, 37–48. [[CrossRef](#)]
15. AlMangour, B.; Grzesiak, D.; Yang, J.-M. Selective laser melting of TiC reinforced 316L stainless steel matrix nanocomposites: Influence of starting TiC particle size and volume content. *Mater. Des.* **2016**, *104*, 141–151. [[CrossRef](#)]
16. Hao, L.; Dadbakhsh, S.; Seaman, O.; Felstead, M. Selective laser melting of a stainless steel and hydroxyapatite composite for load-bearing implant development. *J. Mater. Process. Technol.* **2009**, *209*, 5793–5801. [[CrossRef](#)]
17. Wei, Q.; Li, S.; Han, C.; Li, W.; Cheng, L.; Hao, L.; Shi, Y. Selective laser melting of stainless-steel/nano-hydroxyapatite composites for medical applications: Microstructure, element distribution, crack and mechanical properties. *J. Mater. Process. Technol.* **2015**, *222*, 444–453. [[CrossRef](#)]
18. Kaczmar, J.W.; Pietrzak, K.; Wlosinski, W. The production and application of metal matrix composite materials. *J. Mater. Process. Technol.* **2000**, *106*, 58–67. [[CrossRef](#)]
19. Patankar, S.N.; Tan, M.J. Role of reinforcement in rintering of SiC/316L stainless steel composite. *Powder Metall.* **2000**, *43*, 2–5. [[CrossRef](#)]
20. Olakanmi, E.O.; Cochrane, R.F.; Dalgarno, K.W. A review on selective laser sintering/melting (SLS/SLM) of aluminium alloy powders: Processing, microstructure, and properties. *Prog. Mater. Sci.* **2015**, *74*, 401–477. [[CrossRef](#)]
21. Gu, D.; Wang, H.; Zhang, G. Selective laser melting additive manufacturing of Ti-based nanocomposites: The role of nanopowder. *Metall. Mater. Trans. A Phys. Metall. Mater. Sci.* **2014**, *45*, 464–476. [[CrossRef](#)]
22. Suryanarayana, C.; Ivanov, E.; Boldyrev, V.V. The science and technology of mechanical alloying. *Mater. Sci. Eng. A* **2001**, *304–306*, 151–158. [[CrossRef](#)]
23. Wang, H.; Gu, D. Nanometric TiC reinforced AlSi10Mg nanocomposites: Powder preparation by high-energy ball milling and consolidation by selective laser melting. *J. Compos. Mater.* **2015**, *49*, 1639–1651. [[CrossRef](#)]
24. Yan, A.; Wang, Z.; Yang, T.; Wang, Y.; Ma, Z. Microstructure, thermal physical property and surface morphology of W-Cu composite fabricated via selective laser melting. *Mater. Des.* **2016**, *109*, 79–87. [[CrossRef](#)]
25. Attar, H.; Calin, M.; Zhang, L.C.; Scudino, S.; Eckert, J. Manufacture by selective laser melting and mechanical behavior of commercially pure titanium. *Mater. Sci. Eng. A* **2014**, *593*, 170–177. [[CrossRef](#)]
26. Attar, H.; Bönisch, M.; Calin, M.; Zhang, L.C.; Scudino, S.; Eckert, J. Selective laser melting of in-situ Titanium-Titanium Boride composites: Processing, microstructure and mechanical properties. *Acta Mater.* **2014**, *76*, 13–22. [[CrossRef](#)]
27. Sarma, M.; Grants, I.; Kaldre, I.; Bojarevics, A.; Gerbeth, G. Casting technology for ODS steels-dispersion of nanoparticles in liquid metals. *IOP Conf. Ser. Mater. Sci. Eng.* **2017**, *228*, 012020. [[CrossRef](#)]
28. Alexander, G.B.; Glasgow, T.K. Alexander, G.B.; Glasgow, T.K. A brief history of oxide dispersion-strengthened alloys. In *Mechanical Properties of Metallic Composites*; Ochiai, S., Ed.; CRC Press: Boca Raton, FL, USA, 1993; pp. 5–23.
29. Klueh, R.L.; Shingledecker, J.P.; Swindeman, R.W.; Hoelzer, D.T. Oxide dispersion-strengthened steels: A comparison of some commercial and experimental alloys. *J. Nuclear Mater.* **2005**, *341*, 103–114. [[CrossRef](#)]
30. Bruker Nano GmbH. *QUANTAX EBSD Reinventing Electron Backscatter Diffraction Analysis*; Berlin, Germany, 2017. Available online: https://www.bruker.com/fileadmin/user_upload/8-PDF-Docs/X-rayDiffraction_ElementalAnalysis/Microanalysis_EBSD/Brochures/Bro_quantax_ebsd_16p_en_rev5_lores.pdf (accessed on 17 May 2017).
31. Gu, D.; Shen, Y. Processing conditions and microstructural features of porous 316L stainless steel components by DMLS. *Appl. Surf. Sci.* **2008**, *255*, 1880–1887. [[CrossRef](#)]
32. Yadroitsev, I.; Bertrand, P.; Smurov, I. Parametric analysis of the selective laser melting process. *Appl. Surf. Sci.* **2007**, *253*, 8064–8069. [[CrossRef](#)]
33. Yadroitsev, I.; Smurov, I. Selective laser melting technology: From the single laser melted track stability to 3D parts of complex shape. *Phys. Procedia* **2010**, *5*, 551–560. [[CrossRef](#)]
34. Yadroitsev, I.; Gusarov, A.; Yadroitsava, I.; Smurov, I. Single track formation in selective laser melting of metal powders. *J. Mater. Process. Technol.* **2010**, *210*, 1624–1631. [[CrossRef](#)]
35. Löber, L.; Schimansky, F.P.; Kühn, U.; Pyczak, F.; Eckert, J. Selective laser melting of a beta-solidifying TiNi-B1 titanium aluminide alloy. *J. Mater. Process. Technol.* **2014**, *214*, 1852–1860. [[CrossRef](#)]

36. Dai, D.; Gu, D. Thermal behavior and densification mechanism during selective laser melting of copper matrix composites: Simulation and experiments. *Mater. Des.* **2014**, *55*, 482–491. [[CrossRef](#)]
37. Simchi, A.; Pohl, H. Effects of laser sintering processing parameters on the microstructure and densification of iron powder. *Mater. Sci. Eng. A* **2003**, *359*, 119–128. [[CrossRef](#)]
38. Morgan, R.; Sutcliffe, C.J.; O'Neill, W. Density analysis of direct metal laser re-melted 316L stainless steel cubic primitives. *J. Mater. Sci.* **2004**, *39*, 1195–1205. [[CrossRef](#)]
39. Martienssen, W.; Warlimont, H. (Eds.) *Springer Handbook of Condensed Matter and Materials Data*; Springer: Berlin/Heidelberg, Germany, 2005.
40. Niu, H.J.; Chang, I.T.H. Instability of scan tracks of selective laser sintering of high speed steel powder. *Scripta Mater.* **1999**, *41*, 1229–1234. [[CrossRef](#)]
41. Zheng, B.; Zhou, Y.; Smugeresky, J.E.; Lavernia, E.J. Processing and behavior of Fe-based metallic glass components via laser-engineered net shaping. *Metall. Mater. Trans. A* **2009**, *40*, 1235–1245. [[CrossRef](#)]
42. Saeidi, K.; Gao, X.; Zhong, Y.; Shen, Z.J. Hardened austenite steel with columnar sub-grain structure formed by laser melting. *Mater. Sci. Eng. A* **2015**, *625*, 221–229. [[CrossRef](#)]
43. Zhong, Y.; Liu, L.; Wikman, S.; Cui, D.; Shen, Z. Intragranular cellular segregation network structure strengthening 316L stainless steel prepared by selective laser melting. *J. Nucl. Mater.* **2016**, *470*, 170–178. [[CrossRef](#)]
44. Sun, Z.; Tan, X.; Tor, S.B.; Yeong, W.Y. Selective laser melting of stainless steel 316L with low porosity and high build rates. *Mater. Des.* **2016**, *104*, 197–204. [[CrossRef](#)]
45. Pan, F.; Zhang, J.; Chen, H.-L.; Su, Y.-H.; Kuo, C.-L.; Su, Y.-H.; Chen, S.-H.; Lin, K.-J.; Hsieh, P.-H.; Hwang, W.-S. Effects of rare earth metals on steel microstructures. *Materials* **2016**, *9*, 417. [[CrossRef](#)] [[PubMed](#)]
46. Dutta Majumdar, J.; Pinkerton, A.; Liu, Z.; Manna, I.; Li, L. Microstructure characterisation and process optimization of laser assisted rapid fabrication of 316L stainless steel. *Appl. Surf. Sci.* **2005**, *247*, 320–327. [[CrossRef](#)]
47. Sanaty-Zadeh, A. Comparison between current models for the strength of particulate-reinforced metal matrix nanocomposites with emphasis on consideration of Hall–Petch effect. *Mater. Sci. Eng. A* **2012**, *531*, 112–118. [[CrossRef](#)]
48. Hansen, N. Hall–Petch relation and boundary strengthening. *Scripta Mater.* **2004**, *51*, 801–806. [[CrossRef](#)]



© 2018 by the authors. Licensee MDPI, Basel, Switzerland. This article is an open access article distributed under the terms and conditions of the Creative Commons Attribution (CC BY) license (<http://creativecommons.org/licenses/by/4.0/>).